Real-time particle-by-particle detection of erythrocyte-camouflaged microsensor with extended circulation time in the bloodstream

Wenjun Di[a,1], Xuefei Tan[b,1], Isen Andrew C. Calderon[c], Ashlyn E. Neal Reilly[c], Mark Niedre[b,c], and Heather A. Clark[c,d,2]

[a]Department of Pharmaceutical Sciences, Northeastern University, Boston, MA 02115; [b]Department of Electrical and Computer Engineering, Northeastern University, Boston, MA 02115; [c]Department of Bioengineering, Northeastern University, Boston, MA 02115; and [d]Department of Chemistry and Chemical Biology, Northeastern University, Boston, MA 02115

Edited by John A. Rogers, Northwestern University, Evanston, IL, and approved January 9, 2020 (received for review August 27, 2019)

Personalized medicine offers great potential benefits for disease management but requires continuous monitoring of drugs and drug targets. For instance, the therapeutic window for lithium therapy of bipolar disorder is very narrow, and more frequent monitoring of sodium levels could avoid toxicity. In this work, we developed and validated a platform for long-term, continuous monitoring of systemic analyte concentrations in vivo. First, we developed sodium microsensors that circulate directly in the bloodstream. We used "red blood cell mimicry" to achieve long sensor circulation times of up to 2 wk, while being stable, reversible, and sensitive to sodium over physiologically relevant concentration ranges. Second, we developed an external optical reader to detect and quantify the fluorescence activity of the sensors directly in circulation without having to draw blood samples and correlate the measurement with a phantom calibration curve to measure in vivo sodium. The reader design is inherently scalable to larger limbs, species, and potentially even humans. In combination, this platform represents a paradigm for in vivo drug monitoring that we anticipate will have many applications in the future.

microsensors | erythrocytes | sodium monitoring | diffuse in vivo flow cytometry

Personalized medicine is an emerging concept in healthcare, where drug dosing is tailored to patients to improve treatment response and minimize adverse side effects (1–3). Current dosing regimens typically treat patient populations based on simple metrics such as age, weight, and gender. However, it is well understood that genetic makeup, nutrition, health status, and drug resistance affect drug efficacy and toxicology (4, 5), so that individualized indicators of response are greatly needed (6).

For instance, lithium is still one of the most effective treatments for bipolar disorder (7). However, lithium has a very narrow therapeutic window (8–10), since the therapeutic range (0.6 to 1.2 mM) is close to the minimal levels at which toxicity occurs (1.5 mM) (11). Lithium toxicity can cause acute and chronic side effects to the central nervous and renal systems (9, 12), including decreased sodium reabsorption and sodium depletion in the blood (hyponatremia), ultimately resulting in seizures and even death. As such, continuous and accurate monitoring of systemic sodium levels is critical (13). Currently, most patients receiving lithium treatment undergo periodic blood draws to test sodium levels using blood analyzers (14). However, this is done infrequently (once per week or less), and as such changes in sodium levels that occur over hours and days are not detected (15, 16). Therefore, there is a persistent need for better methods for monitoring of lithium and downstream targets (17) as well as for many other drugs.

One emerging approach is the use optical (fluorescence)-based chemical sensors, which could allow continuous monitoring in vivo over time (18). Previous work by our team and others have shown that optical sensors exhibit long-term stability, reversibility, specificity, sensitivity, and reproducibility (19–22). We previously developed optical sensors that were implanted as "tattoos" in the dermis or subcutaneous tissue to monitor changes in sodium concentration in the interstitial fluid (ISF) (23, 24). This was still problematic, since analyte concentrations in the ISF are not equal to systemic concentrations (25), and in particular usually lag and are higher in the ISF than that in the blood (26). Moreover, the free ion activities in the ISF differ from those of the plasma (27), and the sensors were observed to be cleared out of the skin by macrophages (28), thus restricting sensor lifetime to hours (29).

Motivated by this, in this work, we developed a fluorescent sensor that circulates directly in the bloodstream. Such a sensor would ideally circulate for long periods of time, with clearance half-life of weeks or months. Other groups have studied the circulation kinetics of therapeutic nanoparticles and microparticles and have shown that this is modulated by particle size (30), shape (31), and surface functionality (32) due to multiple clearance mechanisms in the body (33–35). Notably, surface encapsulation of hydrophobic sensing components by PEGylation (36) mitigates particle aggregation, opsonization, and phagocytosis. For example, Huang and coworkers (37) reported that PEGylation resulted in clearance half-life of liposomes of about 5 h. Zhang and coworkers (38) used erythrocyte membranes to camouflage poly(lactic-coglycolic acid) nanoparticles and showed a clearance half-life of 39.6 h. DeSimone and coworkers (39) reported that mimicking red

Significance

We developed and validated an approach for long-term in vivo monitoring of sodium levels in the bloodstream using erythrocyte camouflaging of microsensors combined with noninvasive optical readout of the microsensors while in circulation. Sodium imbalance is an important indicator for toxicity during lithium treatment for bipolar disorder. Lithium treatment has a toxic threshold close to its narrow therapeutic window, which drives the need for long-term continuous monitoring to prevent adverse effects. Our study describes an approach to drug monitoring by using biomimicry and optical reader technology, with wide potential impact toward treatment regimens for bipolar disorder and other conditions.

Author contributions: W.D., X.T., I.A.C.C., M.N., and H.A.C. designed research; W.D., X.T., I.A.C.C., and A.E.N.R. performed research; W.D., X.T., I.A.C.C., A.E.N.R., M.N., and H.A.C. analyzed data; and W.D., X.T., I.A.C.C., A.E.N.R., M.N., and H.A.C. wrote the paper.

The authors declare no competing interest.

This article is a PNAS Direct Submission.

[1]W.D. and X.T. contributed equally to this work.

[2]To whom correspondence may be addressed. Email: h.clark@northeastern.edu.

This article contains supporting information online at https://www.pnas.org/lookup/suppl/doi:10.1073/pnas.1914913117/-/DCSupplemental.

First published February 4, 2020.

blood cell (RBC) size, shape, and rigidity dramatically increased elimination half-life of hydrogel microparticles as have others (40, 41).

Herein, we extended the concept of RBC mimicry to circulating sodium sensors. We used RBC-cloaked, micrometer-sized particles with polymer-free fluorescence sensing cores ("fRBC sensors"). In our fRBC design, we employed and optimized many elements of RBC mimicry simultaneously: RBC membrane exterior, micrometer-sized mimicking of RBC size, and polymer-free interiors. As we show, our fRBC sodium sensors are reversible, stable, and have robust response toward sodium.

Second, we developed a method for externally measuring the fluorescence signals from fRBCs while circulating in the bloodstream, thereby avoiding the need to draw blood samples to "read" sensor activity. We applied a technique that we recently developed—"diffuse in vivo flow cytometry" (DiFC)—which uses highly scattered diffuse light in the near-infrared range to detect and quantify extremely rare, circulating fluorescently labeled cells in the bloodstream (42–45). DiFC is well suited to this application, since it can be applied to large limbs, species, and potentially even humans. The fRBC sensors are designed to be optically compatible with DiFC, so that they can be detected while in circulation at concentrations as low as 1 cell per mL. We used DiFC to track individual fRBCs in mice in vivo and showed that the sensors were detectable for up to 14 d after their injection into the bloodstream, which was 6.5 times longer than more conventionally designed PEGylated sensors. Finally, we measured in vivo sodium concentration in mice using DiFC readout of circulating fRBC sensors and compared our results to a commercial blood analyzer (iSTAT). Fitting the iSTAT and in vivo DiFC measurements to the calibration data obtained from the phantom flow experiment, we measured intensities that indicate Na^+ concentrations lower than 150 mM. The accuracy and variability in our measurements may be further improved upon in the future, but this is outside the scope of the current study. Moreover, we anticipate that our fRBC sensor and optical reader platform could be extended for use with other drugs and drug targets in the future.

Results and Discussion

Sensor Design: Overview. The sensor mechanism for sodium detection is based on the well-developed optode design, validated previously for detection of ions and small molecules (Fig. 1) (19, 22, 46–49). The sensor is composed of a lipophilic polymer-free plasticizer matrix wherein the sensing components are dissolved, encapsulated into particle form with an amphiphilic lipid monolayer (PEG-lipid or RBC membrane) through an oil-in-water emulsion process. The sensing core is composed of a pH-sensitive chromoionophore, an ion-selective but optically inactive sodium ionophore, a reference fluorophore, and a hydrophobic ionic additive to balance the charge within the sensor matrix. Sodium ions in the external aqueous solution are extracted by the sodium ionophore into the hydrophobic sensor core, resulting in the deprotonation of the chromoionophore to maintain charge neutrality within the sensor particle. The change in protonation state of the chromoionophore consequently changes the optical properties of the fluorophore. This ion exchange process is in equilibrium between the sensor and surrounding environment, enabling continuous measurements of sodium fluctuations. A reference fluorophore is added as an internal standard to normalize the response and prevent variability due to sensor concentration or distance from the optical detector. Ratiometric measurements are preferred in sensor design since they facilitate more accurate quantification (49–51). In this design scheme, we used Rhodamine 18 (R18) as the reference fluorophore. R18 is also a pH-sensitive fluorophore but has an inverse response trend compared to chromoionophore III as the pH changes. Thus, using the ratiometric response between these two fluorophores increases the steepness of the slope for the response curves and further increases the sensitivity of the sensor (19, 52–54).

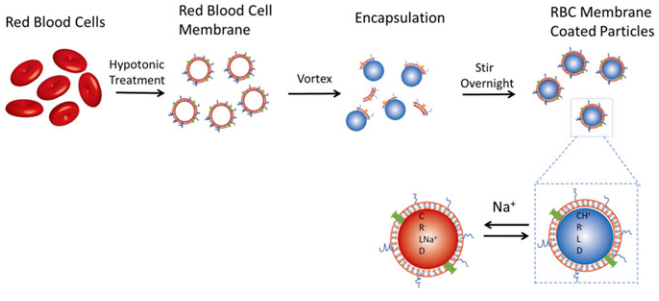

Fig. 1. Schematic of the fRBC sensor mechanism and fabrication process. Optode-based sodium sensor is based on ion extraction mechanism. The sodium optode and the RBC membrane solution were vortexed vigorously and then stirred overnight to homogenize the emulsion and evaporate the organic solvent. C, chromoionophore III; D, reference fluorophore R18; L, sodium ionophore X; R-, ion exchanger NaTFPB.

Size and Zeta Potential Characterization. Images of RBC, fRBC, and PEGylated sensors were taken using bright-field optical microscopy (Fig. 2 *A*–*C*). Sensor particles were spherical with minimal aggregation, indicating a stable suspension of the hydrophobic sensing core in the aqueous environment. This result suggests successful encapsulation of the hydrophobic sensor core with the amphiphilic membrane coating, preventing oil droplet coalescence and particle aggregation into larger irregular structures. ImageJ was used to analyze the bright-field microscopy images of RBC, fRBC, and PEGylated sensors to measure the particle sizes ($n = 100$) (histograms in *SI Appendix*, Fig. S1). The sizes of the sensors are summarized in Fig. 2*D*, with RBCs, fRBC, and PEGylated sensors measuring 6.23 ± 0.66 μm (polydispersity index [PdI] = 0.106), 5.78 ± 1.64 μm (PdI = 0.284), and 6.69 ± 1.97 μm (PdI = 0.294) in diameter, respectively. The fRBC sensors were visualized using transmission electron microscopy (TEM), with size measured (6.19 ± 1.45 μm) that is in good agreement with the measurements obtained using bright-field optical microscopy (*SI Appendix*, Fig. S2).

Using dynamic light scattering, a bimodal population was observed for the fabricated sensors. A mixture of micrometer-sized (5.7 ± 2.2 μm) and nanometer-sized (606.1 ± 360.8 nm) for both fRBC and PEGylated sensors was produced. This is expected since relatively mild conditions (i.e., vortex, stirring) were used in the fabrication process and no harsh treatments (i.e., sonication, extrusion) were used, as severe conditions can break down micrometer-sized architectures into nanometer-sized particles. Producing a monodisperse population of micrometer-sized sensors would be ideal. Nanometer-sized particles produced as a by-product of the fabrication process will be easily cleared from circulation due to size-dependent susceptibility to phagocytosis and endocytosis. Compared to optical nanosensors previously developed in our laboratory, the micrometer-sized sensors are more advantageous for applications cited here, mimicking the size of RBCs. Currently, the fabrication process still needs optimization to better control production of micrometer-sized fRBC sensors with a homogenous size distribution; however, this is beyond the scope of this study.

To further validate successful encapsulation of the sensor core with the RBC membrane, the sensors were also characterized using zeta potential, fluorescence microscopy, and SDS/PAGE. As shown in Fig. 2*D*, the zeta potential was −22.7 ± 3.0 mV for fRBC sensor and −13.2 ± 3.0 mV for PEGylated counterparts. Uncharged PEG chains shield the surface of the particle, thus reducing the available sites for ionization and decreasing the magnitude of the zeta potential measured for PEGylated sensors

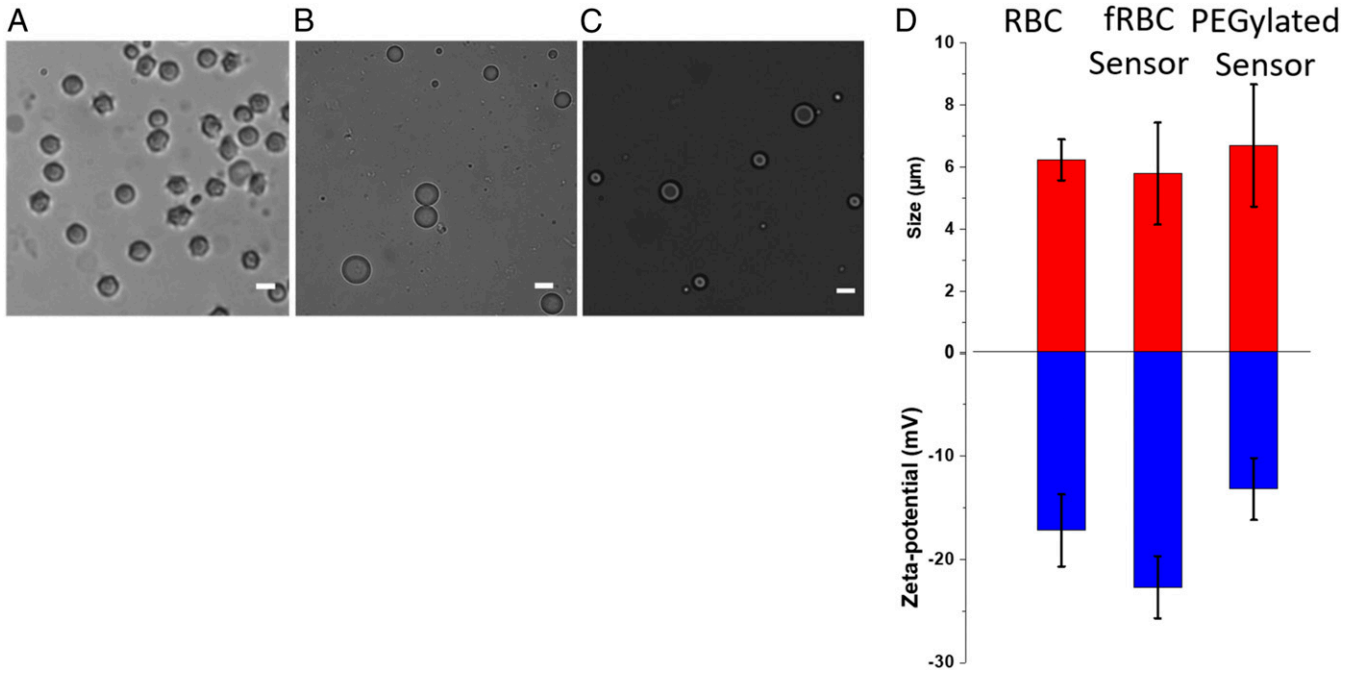

Fig. 2. Morphology, size, and zeta potential of RBCs, fRBC sensors, and PEGylated sensors for comparison. (*A*) Bright-field microscopy image of RBCs with average size of 6.23 ± 0.66 μm ($n = 100$). (*B*) Bright-field microscopy image of fRBC sensors with average size of 5.78 ± 1.64 μm ($n = 100$). (*C*) Bright-field image of PEGylated sensors with average size of 6.69 ± 1.97 μm ($n = 100$). (Scale bar, 5 μm.) (*D*) Size and surface zeta-potential characterization of RBCs, fRBC sensors, and PEGylated sensors. Size distribution histograms are shown in *SI Appendix*, Fig. S1.

compared to fRBC sensors ($P = 0.02$). RBC membranes contain a variety of proteins and lipids that impart a negative surface charge under physiological pH. As measured, the zeta potential of RBCs was −17.2 ± 3.5 mV, similar to that of fRBC sensors ($P = 0.11$), confirming the encapsulation with the RBC membrane. The RBC-mimicking properties of fRBC sensors (i.e., microscale sizing and strong negatively charged surface) should protect the fRBC sensors from being recognized by the reticuloendothelial system (RES) and prevent uptake by tissue. This camouflaging is expected to increase the circulation lifetime of the fRBC sensors compared to PEGylated sensors (55, 56).

Using Alexa Fluor 488-labeled anti-CD47 antibody, the membrane coating of the fRBC sensors was visualized (*SI Appendix*, Fig. S3). After antibody incubation, native CD47 proteins present on the RBC membrane were labeled by the fluorescent antibody, distinguishing the membrane shell from the optode core, thus further corroborating an association of the sensors with the RBC membrane. Furthermore, the protein content of fRBC sensors was also examined using SDS/PAGE analysis (*SI Appendix*, Fig. S4) to determine membrane compositional integrity. The gel image shows that the fRBC sensors have similar protein composition as RBC ghosts, further validating membrane encapsulation of the optode. Maintaining compositional integrity of the membrane is important as the lipids and proteins in the membrane help camouflage the fRBC sensors against biological immune response and prolong the circulation time of the sensors (57–59). It is also known that cell membranes can undergo degradation under long-term storage (60). To investigate the stability of the membrane coating, fRBC sensors were aged and the proteins were analyzed again using SDS/PAGE (*SI Appendix*, Fig. S5). The composition of the RBC membrane changed over time, suggesting that the membrane coating of the fRBC sensors degrades over time. This has functional implications to the fRBC sensors as discussed later when circulation lifetimes of the sensors were characterized.

Response Characterization. The responses of the fRBC and the PEGylated sensors were assessed to determine whether changing the surface coating of the sensors would impact its sensing capability. As sodium concentration increases, the chromoionophore gets increasingly deprotonated, causing the fluorescence intensity of the chromoionophore (680 nm) to decrease. R18 (585 nm), acting as a reference fluorophore, is also pH-responsive and increases in fluorescence intensity with sodium concentration (Fig. 3*A*). The ratiometric measurement reduces the errors associated with sensor concentration. In addition, the incorporation of two pH-sensitive fluorophores with opposite response trends enhances the sensitivity of the sensor, as shown in previous work (19). Using the sigmoidal fit of the calibration curve, the fRBC sensor has a sensitivity of 41% per log unit evaluated at the physiological concentration of sodium (140 mM). The lower limit of detection (LLOD) was 17.9 mM, and the center of the dynamic range was 228 mM. In comparison, the control using PEGylated sensors with equivalent formulation of sodium sensor showed that the responses were comparable. The sensitivity of the PEGylated sensor was 42% per log unit at physiological concentration with a LLOD of 14.9 mM. The center of the dynamic range was 165 mM. The comparison study suggests that the sensor response primarily depends on the formulation of the sensing components and that the biological membrane does not significantly change the sensor response. Although the center of the dynamic range is right-shifted for the fRBC sensor, the response still covers the physiological concentration of sodium.

Reversibility of the sensor response is necessary to track sodium fluctuations continuously, but ion flux could be restricted with a membrane coating lacking functional ion channel dynamics. To investigate response reversibility, the fRBC sensors were placed in dialysis tubing and incubated in alternating solutions of 50 and 150 mM NaCl for 20 min, then measured for fluorescence intensity. In Fig. 3*B*, the sensor response was found to recover up to 90.3% when cycled three times. This recovery confirms that the RBC membrane coating on the fRBC sensor

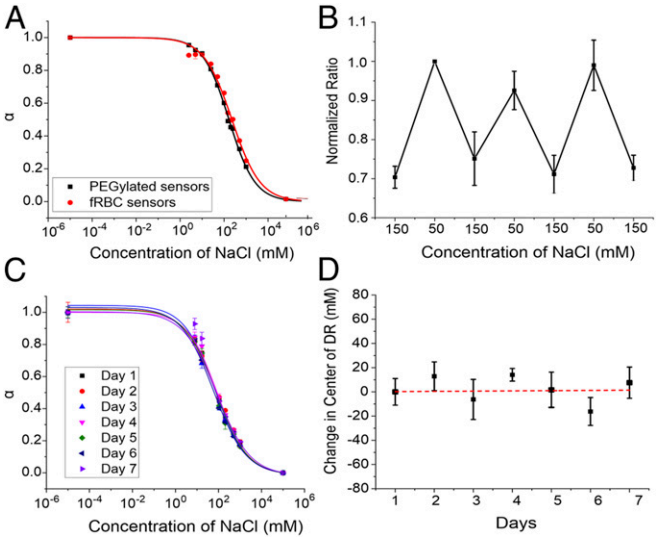

Fig. 3. The fRBC and PEGylated sensor response to sodium, reversibility, and stability. (*A*) Response of the fRBC and PEGylated sensors to sodium in different concentrations. The normalized ratio "α" is derived from the fluorescence emission ratio of CHIII to R18 (680 nm/580 nm). The end points of 10^{-5} and 10^{5} represent the fully protonated and deprotonated states, respectively. (*B*) Reversibility experiment was performed with the fRBC sensors loaded in dialysis tubing. The NaCl solutions with alternating concentrations of 150 and 50 mM were washed through for three cycles. (*C*) Response stability of the fRBC sensors in 10 mM Hepes buffer (pH 7.4) with 10% FBS at 37 °C for 7 d. (*D*) The change in the calculated center of dynamic range of fRBC sensors over 7 d with fitted linear trendline.

does not affect reversibility of the sensing core's response. Moreover, particle-based optode sensors have been used in the past for continuous measurements, demonstrating reversibility over numerous cycles (18, 21). The fRBC sensors are expected to behave similarly to previously developed particle-based optode sensors, considering that RBC surface coatings are leaky and permeable to small cations even without ion channel function (61). From this, we can extrapolate that fRBC sensors should offer limitless reversibility in response, with photobleaching being the eventual limitation.

We previously estimated that the response time of PEGylated particle-based optode sensors is on the order of milliseconds to seconds (6–8), which is easily sufficient for the intended application of monitoring sodium imbalance since the current standard of practice is on hour/day timescales (9–11). The surface coating could potentially affect the response time of the sensors if 1) the membrane coating has a tight seal and relied on ion channels for transport, or 2) the membrane was positively charged, thus causing electrostatic repulsion of sodium ions. Neither condition is applicable here, since both PEGylated and RBC surface coatings are permeable (61, 62), which should preclude any adverse effects to the sensor response time. Moreover, zeta potential measurements of our fRBC sensors indicate that the membrane coating is negatively charged (−22.7 ± 3.0 mV) and thus would not repel sodium ions.

Finally, we assessed the stability of the fRBC sensor response in physiological conditions, namely serum and temperature. Proteins in serum have been known to cause biofouling in particle-based optical sensors, affecting the response of sensors (63), and there is potential for rapid degradation at 37 °C. To assess the stability of the particles, we stored a solution in 10% FBS Hepes buffer at 37 °C and calibrated the sensors every day for 7 d. The calibration curves generated on each day overlay and indicate minimal degradation in signal (Fig. 3*C*), with the center of the dynamic range changing minimally at 0.2 mM/day over 7 d based on a linear trendline fitting (Fig. 3*D*). Compared to buffer solution, smaller change was observed over 7 d (19). Although the change in serum is more significant than that in buffer solution, the actual change of dynamic range is small and still encompasses the range of blood sodium levels under normal (135 to 145 mM) or hyponatremic conditions (115 mM) (64, 65). Thus, the result demonstrated that the fRBC sensor response in serum is stable up to 7 d.

DiFC Measurements of fRBCs in Phantoms. Another major issue was characterization of the fluorescence readout of the fRBC sensors in vivo using DiFC. Our team recently developed DiFC (Fig. 4)—a technique for optical detection of fluorescently labeled circulating cells (42–45) in the bloodstream. DiFC was used for continuous detection of fRBC sensors under flow through an in vitro optical flow-phantom model to mimic in vivo optical properties and blood flow conditions of a large blood vessel in a limb. The fRBC sensors were incubated at varying concentrations of sodium (0, 150, and 300 mM), and the resulting fluorescence intensities were measured with DiFC (n = 4). The distribution of detected peaks from one trial is shown in Fig. 5*A* for each condition as an example and was compared to corresponding measurements obtained using a flow cytometer (FC) (Fig. 5*B*). The mean fRBC fluorescence intensity over four trials (marked with vertical lines in Fig. 5*A*) decreased by 5.2 ± 12.4% and 30.0 ± 21.3% (Fig. 5*C*) versus baseline, when the sodium concentration increased from 0 to 150 and 300 mM, respectively. These were in good agreement with measurements obtained by FC, 23.8 ± 24.8% and 39.2 ± 12.2% reduction for increases to 150 and 300 mM (Fig. 5*C*), respectively. The differences here correspond to the slightly different optical excitation and detection configurations (lasers and filters) of the two systems, and because DiFC measurements are biased toward the more brightly labeled fRBCs, which are externally detectable. These data illustrate that the fluorescence emission of fRBC is quantifiable on a particle-by-particle basis using DiFC.

In Vivo Measurement of fRBC Sensors. DiFC was then utilized to noninvasively study the in vivo circulation kinetics of fRBC sensors in nude mice. The sensors were introduced into mice using retroorbital injection, and the number of fRBCs in circulation

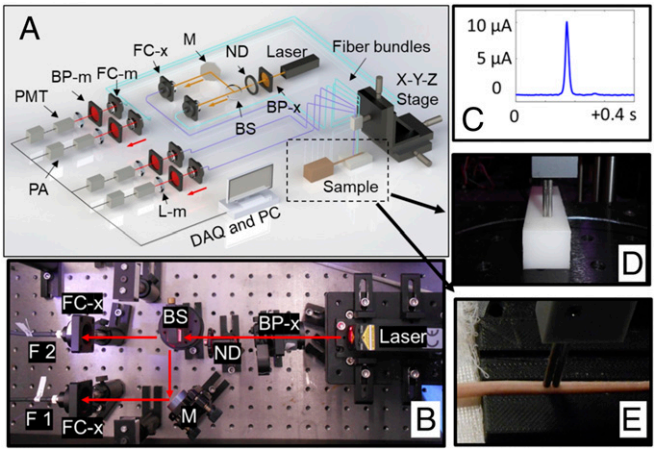

Fig. 4. DiFC system. (*A*) DiFC instrument schematic. (*B*) DiFC system photograph. (BP, bandpass filter; BS, beam splitter; DAQ, data acquisition board; F 1,2, fiber bundle 1 and 2; FC, fiber coupler; M, mirror; ND, neutral density filter; PA, preamplifier; PC, personal computer; PMT, photomultiplier tube. Subscripts: m, emission; x, excitation.) (*C*) Example of a peak that corresponds to a "detected" cell on DiFC. Fiber probes were placed in firm contact with the surface of either a phantom (*D*) or a mouse tail (*E*) during the measurements.

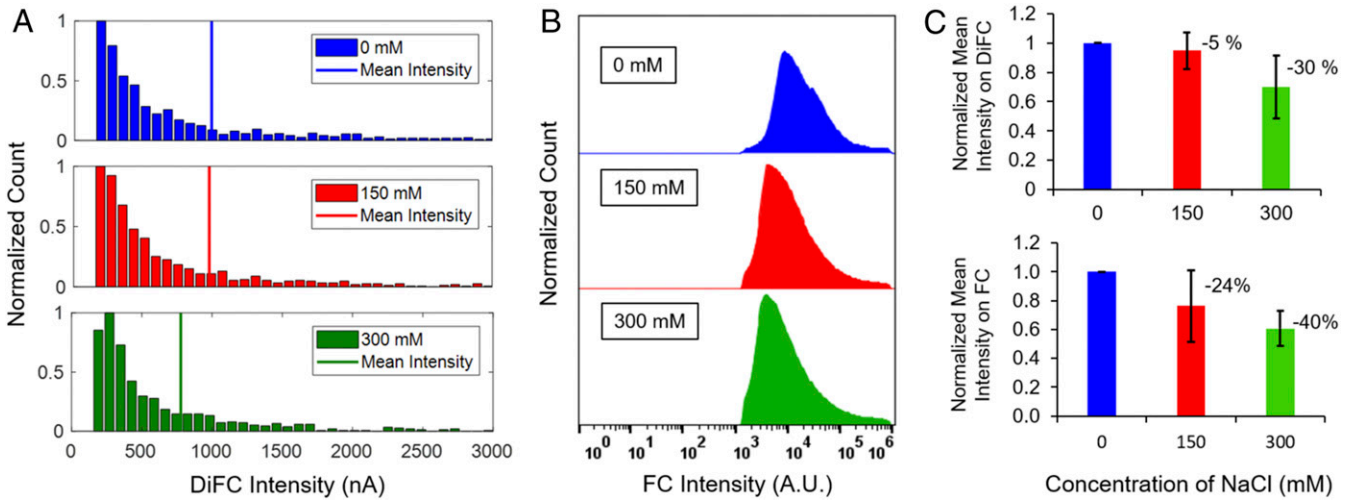

Fig. 5. In vitro response of fRBC sensors to sodium concentrations. Histograms of an example trial of fRBC sensors intensity detected on (*A*) DiFC and (*B*) FC with sodium concentrations of 0, 150, and 300 mM. (*C*) Normalized mean intensity of fRBC sensors over four trials on DiFC or FC with sodium concentrations at 0, 150, and 300 mM.

were measured regularly using DiFC for up to 2 wk. Despite confirming the stability of the sensor response over 7-d storage, cell membranes degrade over time as seen in literature (60) and from gel results obtained prior. Membrane proteins are integral in inducing/preventing biological immune response (58). As such, two different sets of fRBC sensors were prepared, categorized as follows: 1) sensors made from RBC stored for less than 1 wk ("fresh" fRBC sensor), and 2) from RBCs stored for over 1 wk ("old" fRBC sensor). As control, PEGylated sensors were also prepared for performance comparison.

Example 30-s sequences of DiFC data are shown in Fig. 6*A*, where data acquired from injected PEGylated sensors and fresh fRBC sensors at 4, 24, and 72 h after injection are shown. As individual fluorescent sensor passed through the DiFC field of view, fluorescence emission of the individual sensors is detected, producing peaks (as indicated with green markers) on the current-time trace from the DiFC. In all cases, the experiment was terminated when the count rate was below 0.2% of the initial count rate (at $t = 1$ h after injection), or after 14 d, whichever came first. The normalized DiFC data for fresh and old fRBCs and PEGylated control sensors for all mice studies are summarized in Fig. 6*B*.

In the PEGylated sensor group, the count rate decreased to 0.2% after 72 h, indicating that almost all of the PEGylated sensors were cleared from circulation. Similarly, with the old fRBC sensor group, most of the sensors were cleared from circulation after 72 h. However, for the fresh fRBC sensor group, count rates only decreased to below 0.2% at 336 h (14 d) after injection. While the count rate for all of the sensors tested decreased significantly over the 72-h period, the fresh fRBC sensors stayed in circulation significantly longer than the PEGylated and the old fRBC sensors. Clearance profiles of sensors in individual animals are shown in *SI Appendix*, Fig. S6.

We applied a two-compartment pharmacokinetic model that best fits the datasets acquired to calculate for the elimination half-life of each group of sensors. The half-lives were calculated to be 5.6 ± 1.7, 10.3 ± 3.1, and 36.3 ± 20.4 h for the PEGylated sensors, old fRBC sensors, and fresh fRBC sensors, respectively (Fig. 6*C*). The increased circulation half-life of old fRBC sensors is not significant when compared to PEGylated sensors ($P = 0.056$). Notably, the fresh fRBC sensors have significantly longer half-life compared to both the PEGylated ($P = 0.024$) and the old fRBC sensors ($P = 0.016$). Using SDS/PAGE analysis (*SI Appendix*, Fig. S5), we observed that protein degradation on the surface of RBCs occurred when the blood was stored over the course of weeks. Components in the membrane such as membrane proteins (e.g., CD47) play a key role in cellular signaling, preventing phagocytosis or immune response (66–69). Age-based degradation of these components could lead to loss in sensor cloaking and correlate with the observed decrease in circulation lifetime and half-life of the old fRBC sensors compared to the fresh fRBC sensors.

In addition to confirming the long-term circulation of fRBC sensors in the bloodstream, we also used fresh fRBC sensors in conjunction with particle-by-particle DiFC measurements to estimate the in vivo sodium concentrations in mice ($n = 3$). We first performed calibration of in vivo DiFC data by measuring fRBC intensities in a reference flow phantom at Na^+ concentrations of 0, 150, and 300 mM. For comparison, we also measured the Na^+ concentration in mouse blood drawn immediately following the DiFC measurements using a commercial blood analyzer (iSTAT; CHEM8+ cartridge; Abbott). When the particle-by-particle in vivo DiFC measurements were plotted against the phantom calibration data (Fig. 6*D*), the normalized mean intensity indicated that the in vivo Na^+ concentration was slightly below 150 mM, according to the calibration fitted with a sigmoidal curve. This was in good general agreement with the independent in vivo Na^+ measurements made using the iSTAT system. We note that the relatively high interexperimental variability observed in these measurements may be attributed to variability associated with probe alignment, tissue depth, and sensor batch-to-batch intensity differences. We plan to upgrade the DiFC reader (in progress) to enable ratiometric measurements that we anticipate will reduce variability from the factors above. Furthermore, improvements in the fabrication of the sensors may be explored to decrease interbatch variations in size and brightness. However, overall, these data provide clear proof-of-concept for measuring systemic Na^+ in vivo using the current sensor and detection system.

Although sensor response stability has been established in previous experiments, there are additional challenges that can affect accurate detection of fRBC sensors (i.e., photobleaching, biofouling, etc.). Given that the mean detected signal-to-noise ratio (SNR) in mice in vivo was 26 dB, and assuming a minimum detectable SNR of 15 dB, using our current design individual sensors could lose on average up to 72% brightness and still be

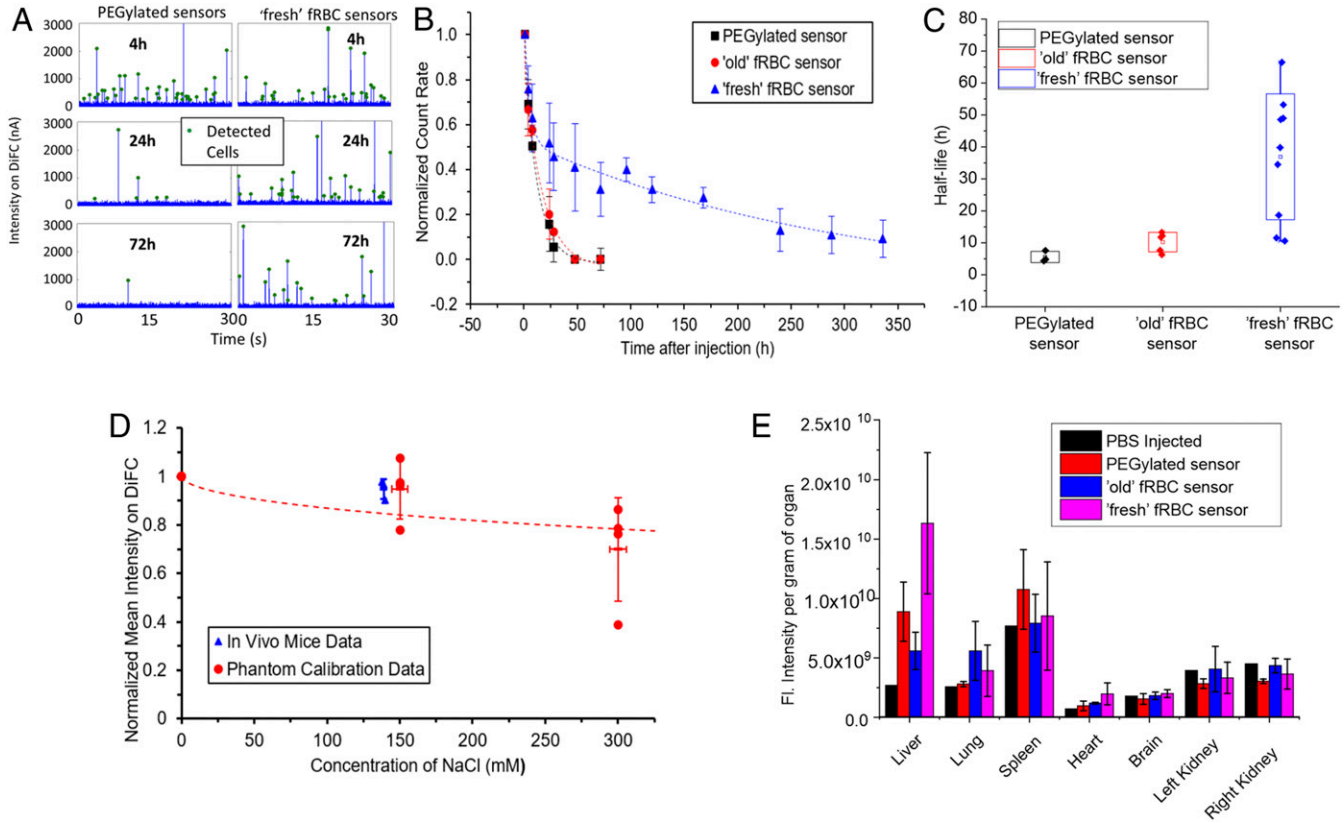

Fig. 6. The in vivo circulation time and half-life of the fRBC and PEGylated sensors and its biodistribution. (*A*) Examples of detected sensors measured with DiFC. Example data were taken from two mice, either from a mouse injected with PEGylated sensors (*Left*) or a mouse injected with fresh fRBC sensors (*Right*), at time points 4, 24, and 72 h. (*B*) The sensor signals were detected by DiFC in nude mice at 635-nm excitation at 1, 4, 8, 24, 28, 48, and 72 h or later at 96, 120, 168, 240, 288, and 336 h (14 d) ($n = 3$, 5, and 9 for PEGylated, old fRBC sensor, and fresh fRBC sensor, respectively). (*C*) Half-life comparison study according to a two-compartment pharmacokinetic model. The line in each group represents the mean value. (*D*) In vivo Na^+ measurements on live mice ($n = 3$) as measured by DiFC scanning of fresh fRBC sensors fitted against phantom calibration curve. (*E*) The fluorescence intensities of PEGylated, old and fresh fRBC sensors localized in the organs were quantified using the in vivo imaging system (IVIS).

detectable. We also note that photobleaching is expected to be minimal since individual fRBCs dwell in the DiFC field of view for less than a second, on average once every 10 min (44).

Elimination of Sensors from the Bloodstream. Finally, we investigated the biodistribution of old and fresh fRBC sensors and PEGylated sensors in mice. Organs were harvested at the end of the elimination phase. This was defined as the time point when the measured fRBC count rate (using DiFC) dropped below 0.2% of the initial value. After the sensors were eliminated from the bloodstream, the organs (i.e., brains, hearts, lungs, livers, kidneys, and spleens) were harvested, washed, and imaged using IVIS Lumia II. Fig. 6*E* exhibits the fluorescence signal per gram of organ. After taking the organ mass into account, it was discovered that the primary elimination pathway of the sensors is through the liver, with significant difference compared to the saline-injected groups ($P = 0.04$). The liver had the highest fluorescence intensity, indicating that the sensing components from the sensors have accumulated in this organ. The lungs and spleen also had some fluorescence signals but not significantly different from the control group (saline). This result suggests that the sensors were ultimately taken up by the RES after elimination from the bloodstream, regardless of which sensor group. Observing that the major elimination pathway of the fRBC sensor group goes through the liver is coherent with previous work reporting that RBC-derived vesicles (~85%) were removed from plasma to the liver, primarily through Kupffer cells and other macrophages of the mononuclear-phagocyte system (70–72). Thus, the liver, especially Kupffer cells, play vital roles in the elimination of the fRBC sensors, although fractionation studies are needed for validation. Despite the difference in pharmacokinetic profiles for the different sensor groups, the ultimate elimination pathways are similar. The fresh fRBC surface membrane coating is beneficial as it extends the circulation time of the sensors in the bloodstream while retaining its sensing and elimination pathway.

This type of sensor has been used previously, and no apparent toxicity was noted (73). However, it is conceivable that there may be specific organ toxicity that would arise from a systemic injection and subsequent collection in the liver. The plasticizer dioctylsebacate (DOS) used in the current formulation is widely used and relatively nontoxic (74). Recent work by Crespo and coworkers (73) studied the cytotoxicity of various ionophore-based membranes, showing little or no cytotoxic effects in cell culture. Although this sensor composition is promising in early studies, chronic exposure, specific organ toxicity, and metabolic effects are key areas that need further investigation.

Conclusions

In summary, we have successfully developed a fluorescence-based sensor platform for direct measurement of systemic sodium levels. The fRBC sensors were responsive to sodium ions with a dynamic range of 46.1 to 918.4 mM. The sensitivity is 41% change per log unit in the physiological range of sodium in vitro. The response was reversible between alternating concentrations of sodium from 50 to 150 mM for over three cycles with 90.3%

recovery to the baseline. Moreover, the sensor response was stable in 10% FBS as evaluated for 7 d with the center of dynamic range changing minimally at 0.2 mM/day. In addition to the analytical performances mentioned, a sensor for continuous in vivo monitoring must be translatable from in vitro to in vivo, overcoming challenges of tissue scattering, stability in biological environment, reversibility, and/or limits of detection (75).

In this paper, we overcame the limitation of "reading" our sensor directly into the bloodstream by using a specialized optical instrument (DiFC) to externally detect and quantify fRBC sensor activity. We showed that the sensors were still detectable 14 d after injection. Using the RBC membrane as coating strategy gives the fRBC sensor significantly longer circulation time compared to its PEGylated counterparts. Our use of the erythrocyte coating increased the sensor circulation half-life by a factor of 6.5. Furthermore, we were able to measure in vivo sodium concentrations using our fRBC sensors with DiFC optical readout, with a calibration fitting that was in good general agreement with expected trend with observed interexperimental variability.

Our results also illustrate the importance of using fresh blood (RBCs) for coating of the particles to avoid degradation of key molecules and/or proteins in the membrane that help increase the sensor circulation time. We anticipate that with the refinement of our fabrication method, we can further extend the circulation lifetime of the sensors. Future studies will involve identification of the proteins in the SDS/PAGE bands to better understand how to control sensor circulation time and adding the key elements to prevent them from degrading.

In the future, we also plan to incorporate ratiometric fluorescence measurements into the DiFC reader to better quantify the particle-by-particle fluorescence intensity. Ratiometric measurements will provide a reference measurement to better account for tissue optical properties and particle-to-particle variation in sensor intensity [similar to our previous work in skin tattoos (19)], to enable better quantification of sodium levels in vivo and reduce variability in measurements. We also plan to improve the detection sensitivity of DiFC for fRBCs by increasing numerical aperture and employing lock-in detection techniques. In addition to sodium, we expect that our fRBC platform could be extended to monitoring a wide range of drug and drug targets including lithium and glucose.

Materials and Methods

Data Availability. Data have been made available on Blackfynn Discover (https://discover.blackfynn.com/) and are filed under the title of the manuscript.

Materials. Rat RBCs were obtained from Innovative Research. Optode mixture components were as follows: chromoionophore III (Sigma-Aldrich), bis(2-ethylhexyl) sebacate (DOS) (Sigma-Aldrich), sodium tetrakis[3,5-bis(trifluoromethyl) phenyl]borate (NaTFPB) (Sigma-Aldrich), sodium ionophore X (Sigma-Aldrich), octadecyl rhodamine B chloride (R18) (Thermo Fisher Scientific), and dichloromethane (DCM) (anhydrous; ≥99.8%; Sigma-Aldrich). The pH 7.4, 10 mM 4-(2-hydroxyethyl)-1-piperazineethanesulfonic acid (Hepes) (BioPerformance Certified; ≥99.5% [titration]; cell culture tested; from Sigma-Aldrich) buffer was prepared in distilled water. All other reagents used were purchased as follows: hydrochloric acid AR (35 to 37%) (Sigma-Aldrich), Trizma base (≥99.0% [T]; Sigma-Aldrich), sodium chloride (BioXtra; ≥99.5% [AT]; Sigma-Aldrich), and 1,2-distearoyl-*sn*-glycero-3-phosphoethanolamine-*N*-[methoxy(polyethylene glycol)-550] (ammonium salt) (PEG-Lipid; Avanti Lipids).

Methods.

Preparation of RBC membrane. RBC membranes are prepared based on published protocol (38). Four milliliters of fresh rat RBCs were washed for three times in 1× PBS by centrifugation at 600 × *g* for 10 min at 4 °C. Then, the washed RBCs were suspended in 0.25× PBS in an ice bath for 20 min. After the hypotonic treatment, the supernatant organelles and hemoglobin were removed by centrifugation at 10,000 × *g* for 20 min at 4 °C. The pink pellet RBC membranes were prepared by rinsing with cold 1× PBS solution for three times. Finally, 4 mL of 10 mM Hepes buffer solution was added to RBC membrane solution in a 2-tri glass vial for further use.

Optode preparation. The optode mixture was prepared in a 2-mL glass vial. 1.5 mg of sodium ionophore X, 0.5 mg of chromoionophore III, 2.0 mg of NaTFPB, 0.1 mg of R18, and 200 μL of plasticizer DOS were added into the glass vial with 500 μL of DCM. For each batch of sodium sensor particles, we used 100 μL of optode mixture solution.

Preparation of RBC membrane-coated particles. Ten micrograms of PEG-lipid and the RBC membrane in 10 mM Hepes solution were vortexed for 30 s. One hundred microliters of sodium optode mixture was added to 400 μL of DCM. Afterward, the hydrophobic phase solution was added to the RBC membrane solution while being vortexed vigorously for 5 min. Then, the mixed emulsion solution was stirred on a magnetic stir plate with the lid off overnight to evaporate the organic solvent DCM. After the stirring, the emulsion solution was washed twice with 10 mM Hepes buffer to remove all of the free RBC membrane and free optode solution. After the washing step, the fRBC sensor solution was centrifuged at 300 × *g* to remove any bulk particles.

Characterization of size, zeta potential, and encapsulation. The zeta-potential measurements were performed using 90Plus Particle Size Analyzer (Brookhaven Instrument Corporation) in 10 mM Hepes (pH 7.4) buffer solution. The particle size was estimated using images captured with bright-field optical microscopy (Olympus fluorescence microscope) and analyzed using ImageJ (n = 100 particles). To characterize the morphology and membrane encapsulation, fRBC sensors were negatively stained with NanoW and then visualized using the FEI Tecnai F20 Cryo-Bio 200-kV FEG TEM (Center of Nanoscale of System at Harvard University). Grids were glow discharged for 30 s with a HDT-400 hydrophilic treatment device (Jeol Datum). The sensor sample was prepared with single-droplet method on carbon-coated, 300 mesh copper TEM grids and imaged at 200 eV. TEM image was adjusted for contrast with Gatan Microscopy Suite 3 software (Gatan). In addition, a fluorophore-free version (chromoionophore III and R18 not added in mixture) of the fRBC sensor was prepared, then incubated with Alexa Fluor 488-labeled anti-CD47 (Santa Cruz Biotechnology) (5 μg/mL) overnight under 4 °C. After antibody labeling, the sensors were then imaged using confocal microscopy (Zeiss LSM880 in the Institute for Chemical Imaging of Living Systems at Northeastern University). SDS/PAGE analysis was also performed to investigate membrane composition of the fRBC sensors. RBC membrane and the fRBC sensors were prepared and dispersed in SDS sample buffer (Invitrogen). The samples were run on a NuPAGE Novex 4 to 12% Bis-Tris gel, 1.0 mm × 12-well with Mini Gel Tank in MES running buffer using PowerEase 90-W Electrophoresis power System (Invitrogen). The samples were run at 150 V for 1 h, and the resulting polyacrylamide gel was stained in SimplyBlue (Invitrogen) for 1 h and washed for visualization (Bio-Rad ChemiDoc Imaging System).

Response calibration, reversibility, and stability. Freshly fabricated fRBC sensors were calibrated toward sodium in 10 mM Hepes buffer solution (pH 7.4) with fluorescence measurements taken using Spectramax M3 plate reader (Molecular Device) in bottom read mode. One hundred microliters of fRBC sensor solution was added to each well and mixed with 100 μL of NaCl solution with different concentrations ranging from 0 to 2,000 mM (pH 7.4) in a clear-bottom 96-well plate. The final concentration in each well is one-half the NaCl stock solutions. Five hundred millimolar NaOH and HCl were used to represent the fully deprotonated and protonated states, respectively. The fluorescence intensities for CHIII (ex: 639 nm; em: 680 nm) and R18 (ex: 555 nm; em: 580 nm) were measured. The fluorescence ratio for CHIII:R18 was calculated as follows:

$$R = \frac{CHIII}{R18}$$

The ratio of CHIII and R18 was further normalized by computing α:

$$\alpha = \frac{Rp - Ri}{Rp - Rd}$$

where Ri is the ratio at each NaCl solution. Rp represents the ratio when the sensors were fully protonated, and Rd is the ratio when they were fully deprotonated. α is defined as the degree of protonation. The calibration curve was plotted in log scale of NaCl concentration to α. The 10^{-5} and 10^{5} represent the α values of HCl and NaOH, respectively. We set the numbers to best fit the sigmoidal curve. Finally, the dynamic range and K_d were calculated based on the dose–response equation using Origin software.

For reversibility experiments, the dialysis tubing with the fRBC sensors was sealed on both ends with curing epoxy and placed on a Petri dish with water-curing epoxy. The dialysis tubes were incubated with solutions of 50 and

150 mM NaCl for 20 min, performed in three cycles. The fluorescence images of the fRBC sensors in the tubing were acquired using the in vivo imaging system (IVIS). Images were analyzed with the region of interest (ROI) using the IVIS system software, and the ROI definitions for both CHIII and R18 channels were the same. The ratio of CHIII to R18 was finally calculated as the ratiometric measurement.

To characterize the stability of fRBC sensors, we evaluated the responses of the sensor in 10% FBS over 7 d. The fRBC sensors were stored in 10 mM Hepes buffer solution (pH 7.4) with 10% FBS at 37 °C. For the calibration of response, fluorescence intensities of CHIII and R18 were measured with a plate reader.

DiFC. Design and validation of the DiFC instrument and signal processing algorithms were described in detail previously (44, 45). DiFC is designed to detect very rare, fluorescently labeled cells moving in circulation in highly scattering biological tissue (42–45). Briefly, DiFC (Fig. 4 *A* and *B*) uses a pair of optical fiber bundles that are placed in direct contact with the skin (or optical phantom) surface. The fibers bundle consists of a central "source" fiber and eight fluorescence collection fibers, as well as integrated optical filters and collection lens. As each fluorescently labeled fRBC sensor passes through the field of view of the probe, a transient fluorescence pulse is generated and detected (Fig. 4*C*). Signal processing algorithms remove the background and distinguish moving peaks from motion artifacts. The peak amplitude (height) reflects the measured fluorescence intensity (in units of current of PMT output [nanoamperes]), which is linearly related to the brightness of individual fRBC sensors. After data collection, we analyzed DiFC data to report the count rate (counts per minute) and average peak amplitude (nanoamperes) during scanning.

Experiments in phantoms in vitro. The fluorescence intensity (brightness) of fRBC sensors in the presence of different concentrations of sodium (NaCl) was first studied in a phantom model (Fig. 4*D*) using our DiFC instrument and a commercial FC (Attune NxT, Thermo Fisher Scientific). A 635-nm excitation laser and a 695/40-nm bandpass emission filter were used on the FC, to match the optics settings on DiFC. A block of high-density polyethylene, with dimensions $5 \times 2 \times 1$ cm^3, was used to mimic mouse tissue. We previously measured the optical properties of this block as $\mu`_s = 9.95$ cm^{-1}, $\mu_a = 0.036$ cm^{-1}, at 690 nm, which is close to the reported values for biological tissue. A strand of Tygon tubing (TGY-010-C; Small Parts, Inc.) embedded inside a fine hole drilled inside the phantom 0.75 mm from the surface was used to mimic a blood vessel. The inner diameter of the tubing is 250 μm, and the outer diameter is 750 μm. Samples were placed in a 1-mL syringe attached to the Tygon tubing, and then pumped with a microsyringe pump (70-2209; Harvard Apparatus) to produce a flow at a controlled linear speed of 39 mm/s. fRBC sensors were suspended at concentrations of 500 to 800 per mL in 10 mM Hepes solution (pH 7.4) and coincubated with different concentrations of NaCl (0, 150, and 300 mM). The fRBC sensors were counted with DiFC, and the peak intensity (brightness) of the detected fRBC sensors was calculated for each concentration with a minimum threshold of 250 nA and a maximum threshold of 10,000 nA. The minimum threshold was used to define detectable signals, and the maximum threshold was used to eliminate possible cells clumping. Solutions of fRBC sensors with the same sodium concentration were then run through FC to validate the intensity variations. Fluorescent microspheres Flash Red, brightness level 4 (FR4; Bangs Laboratory, Inc.) were also run on both DiFC and FC as reference beads to estimate the thresholds applied on both systems. The corresponding minimum threshold applied on FC was 1,500 arbitrary units. One thousand to 2,000 fRBCs were counted on DiFC, while 20,000 to 200,000 fRBC sensors were counted on FC for each concentration.

In vivo measurement of fRBC sensors using DiFC. All mice were handled in accordance with Northeastern University's Institutional Animal Care and Use Committee (IACUC) policies on animal care. Animal experiments were carried out under Northeastern University IACUC protocol no. 17-1141R-A3. All experiments and methods were performed with approval from and in accordance with relevant guidelines and regulations of Northeastern University IACUC. We performed DiFC measurements in three groups of mice to investigate the circulation lifetime of the fRBC sensors in the bloodstream. A total number of 20 female athymic NCr-nu/nu nude mice aged 10 to 11 wk (Charles River Labs) were used in this study.

Each mouse was injected with 10^5 sensors suspended in 100 μL of 10 mM Hepes solution (pH 7.4) via retroorbital injection. Mice were scanned by DiFC system at multiple time points after the injection as below. During each scan, the injected mouse was kept under isoflurane, and the tail was secured with a custom-made holder. The DiFC probe was placed on the ventral surface of the tail about 3 cm from the mouse body, approximately above the artery. The DiFC probe was placed in firm contact with the skin, to prevent motion artifacts during scanning (Fig. 4*E*). A heating pad was also placed over the exposed area of the mouse tail during the scanning to maintain blood flow in the tail.

For investigating sensor clearance, mice were divided into three groups as follows: 1) group 1, PEGylated sensor ($n = 3$); mice were injected with PEGylated sensors as a control; mice were scanned for 30 min, at time points starting 1, 4, 8, 24, 28, 48, and 72 h after injection; 2) group 2, old fRBC sensor ($n = 5$); mice were injected with fRBC sensors fabricated from blood stored over 1 wk; mice were scanned for 30 min, at time points starting 1, 4, 8, 24, 28, 48, and 72 h after injection; and 3) group 3, fresh fRBC sensor ($n = 9$); mice were injected with fRBC sensors fabricated from blood stored less than 1 wk; mice were scanned for 30 min at time points 1, 4, 8, 24, 28, 48, 72, 96, 120, 168, 240, 288, and 336 h after injection.

All mice were then euthanized immediately after experiments. Mice were dissected and organs including liver, lungs, spleen, kidney, heart, and brain were collected for the assessment of biodistribution of the PEGylated, old and fresh fRBC sensors. Saline group represents animal that was injected with saline solution only as a negative control ($n = 1$).

For measuring in vivo Na^+ using DiFC. Fresh fRBC sensors were prepared as previously described and measured using the DiFC under the phantom model, calibrating intensities against 0, 150, and 300 mM NaCl solutions in 10 mM Hepes solution (pH 7.4). After fRBC sensor calibration, mice ($n = 3$) were anesthetized under isoflurane, and blood was subsequently extracted using submandibular blood draw technique. One hundred microliters of the blood was loaded into a CHEM8+ cartridge and analyzed using the iSTAT (Abbot) blood analyzer to measure blood sodium concentration. Mice were injected with fRBC sensors fabricated from blood stored less than 1 wk and scanned for 1 h after injection, as previously described. Normalized intensities (normalized to the brightness of the sensors in the absence of NaCl) measured from the animal scanning were then fitted to the calibration curve generated from the phantom model, fitted using a sigmoidal curve. All mice were then euthanized immediately after experiments.

ACKNOWLEDGMENTS. This work was supported by the NIH (R01 EB024186; National Institute of Biomedical Imaging and Bioengineering). We thank Dr. Guoxin Rong for rigorous editing and proofreading the manuscript and Fernando Ivich for assisting in running the DiFC experiments.

1. M. A. Hamburg, F. S. Collins, The path to personalized medicine. *N. Engl. J. Med.* **363**, 301–304 (2010).
2. N. J. Schork, Personalized medicine: Time for one-person trials. *Nature* **520**, 609–611 (2015).
3. I. D. Wilson, Drugs, bugs, and personalized medicine: Pharmacometabonomics enters the ring. *Proc. Natl. Acad. Sci. U.S.A.* **106**, 14187–14188 (2009).
4. J. K. Nicholson, Global systems biology, personalized medicine and molecular epidemiology. *Mol. Syst. Biol.* **2**, 52 (2006).
5. D. W. Bianchi, From prenatal genomic diagnosis to fetal personalized medicine: Progress and challenges. *Nat. Med.* **18**, 1041–1051 (2012).
6. R. Paradiso, A. M. Bianchi, K. Lau, E. P. Scilingo, PSYCHE: Personalised monitoring systems for care in mental health. *Conf. Proc. IEEE Eng. Med. Biol. Soc.* **2010**, 3602–3605 (2010).
7. R. H. Lenox, R. K. McNamara, R. L. Papke, H. K. Manji, Neurobiology of lithium: An update. *J. Clin. Psychiatry* **59** (suppl. 6), 37–47 (1998).
8. R. Boton, M. Gaviria, D. C. Batlle, Prevalence, pathogenesis, and treatment of renal dysfunction associated with chronic lithium therapy. *Am. J. Kidney Dis.* **10**, 329–345 (1987).
9. R. F. McKnight *et al.*, Lithium toxicity profile: A systematic review and meta-analysis. *Lancet* **379**, 721–728 (2012).
10. M. Schou, Lithium studies. 1. Toxicity. *Acta Pharmacol. Toxicol. (Copenh.)* **15**, 70–84 (1958).
11. R. T. Timmer, J. M. Sands, Lithium intoxication. *J. Am. Soc. Nephrol.* **10**, 666–674 (1999).
12. W. M. Bennett, Drug interactions and consequences of sodium restriction. *Am. J. Clin. Nutr.* **65** (suppl. 2), 678S–681S (1997).
13. F. J. McMahon, T. R. Insel, Pharmacogenomics and personalized medicine in neuropsychiatry. *Neuron* **74**, 773–776 (2012).
14. M. E. Meyerhoff, In-vivo blood-gas and electrolyte sensors—progress and challenges. *Trac Trend. Anal. Chem.* **12**, 257–266 (1993).
15. J. N. Forrest, Jr, *et al.*, Superiority of demeclocycline over lithium in the treatment of chronic syndrome of inappropriate secretion of antidiuretic hormone. *N. Engl. J. Med.* **298**, 173–177 (1978).
16. N. Collins, T. R. E. Barnes, A. Shingleton-Smith, D. Gerrett, C. Paton, Standards of lithium monitoring in mental health Ttrusts in the UK. *BMC Psychiatry* **10**, 80 (2010).
17. M. Nederlof *et al.*, Monitoring of patients treated with lithium for bipolar disorder: An international survey. *Int. J. Bipolar Disord.* **6**, 12 (2018).
18. G. Rong *et al.*, Imaging sodium flux during action potentials in neurons with fluorescent nanosensors and transparent microelectrodes. *ACS Sens.* **3**, 2499–2505 (2018).

19. T. T. Ruckh, A. A. Mehta, J. M. Dubach, H. A. Clark, Polymer-free optode nanosensors for dynamic, reversible, and ratiometric sodium imaging in the physiological range. *Sci. Rep.* **3**, 3366 (2013).
20. A. Sahari, T. T. Ruckh, R. Hutchings, H. A. Clark, Development of an optical nanosensor incorporating a pH-sensitive quencher dye for potassium imaging. *Anal. Chem.* **87**, 10684–10687 (2015).
21. G. Rong, E. H. Kim, K. E. Poskanzer, H. A. Clark, A method for estimating intracellular ion concentration using optical nanosensors and ratiometric imaging. *Sci. Rep.* **7**, 10819 (2017).
22. J. Dubach, S. Das, A. Rosenzwelg, H. Clark, Novel intracellular sodium nanosensors to study sodium dynamics in cardiomyocytes. *Circulation* **118**, S399 (2008).
23. K. J. Cash, C. Li, J. Xia, L. V. Wang, H. A. Clark, Optical drug monitoring: Photoacoustic imaging of nanosensors to monitor therapeutic lithium in vivo. *ACS Nano* **9**, 1692–1698 (2015).
24. K. J. Cash, H. A. Clark, In vivo histamine optical nanosensors. *Sensors (Basel)* **12**, 11922–11932 (2012).
25. M. Gilányi, C. Ikrényi, J. Fekete, K. Ikrényi, A. G. Kovách, Ion concentrations in subcutaneous interstitial fluid: Measured versus expected values. *Am. J. Physiol.* **255**, F513–F519 (1988).
26. G. Szabó, Z. Magyar, Electrolyte concentrations in subcutaneous tissue fluid and lymph. *Lymphology* **15**, 174–177 (1982).
27. N. Fogh-Andersen, B. M. Altura, B. T. Altura, O. Siggaard-Andersen, Composition of interstitial fluid. *Clin. Chem.* **41**, 1522–1525 (1995).
28. A. Aderem, D. M. Underhill, Mechanisms of phagocytosis in macrophages. *Annu. Rev. Immunol.* **17**, 593–623 (1999).
29. J. Heyes, K. Hall, V. Tailor, R. Lenz, I. MacLachlan, Synthesis and characterization of novel poly(ethylene glycol)-lipid conjugates suitable for use in drug delivery. *J. Control. Release* **112**, 280–290 (2006).
30. D. S. Kohane, Microparticles and nanoparticles for drug delivery. *Biotechnol. Bioeng.* **96**, 203–209 (2007).
31. Y. Geng *et al*., Shape effects of filaments versus spherical particles in flow and drug delivery. *Nat. Nanotechnol.* **2**, 249–255 (2007).
32. D. C. Drummond, O. Meyer, K. Hong, D. B. Kirpotin, D. Papahadjopoulos, Optimizing liposomes for delivery of chemotherapeutic agents to solid tumors. *Pharmacol. Rev.* **51**, 691–743 (1999).
33. J. A. Champion, A. Walker, S. Mitragotri, Role of particle size in phagocytosis of polymeric microspheres. *Pharm. Res.* **25**, 1815–1821 (2008).
34. M. K. Balaconis, K. Billingsley, M. J. Dubach, K. J. Cash, H. A. Clark, The design and development of fluorescent nano-optodes for in vivo glucose monitoring. *J. Diabetes Sci. Technol.* **5**, 68–75 (2011).
35. K. Billingsley *et al*., Fluorescent nano-optodes for glucose detection. *Anal. Chem.* **82**, 3707–3713 (2010).
36. J. M. Dubach, D. I. Harjes, H. A. Clark, Fluorescent ion-selective nanosensors for intracellular analysis with improved lifetime and size. *Nano Lett.* **7**, 1827–1831 (2007).
37. A. L. Klibanov, K. Maruyama, V. P. Torchilin, L. Huang, Amphipathic polyethyleneglycols effectively prolong the circulation time of liposomes. *FEBS Lett.* **268**, 235–237 (1990).
38. C. M. J. Hu *et al*., Erythrocyte membrane-camouflaged polymeric nanoparticles as a biomimetic delivery platform. *Proc. Natl. Acad. Sci. U.S.A.* **108**, 10980–10985 (2011).
39. T. J. Merkel *et al*., Using mechanobiological mimicry of red blood cells to extend circulation times of hydrogel microparticles. *Proc. Natl. Acad. Sci. U.S.A.* **108**, 586–591 (2011).
40. E. T. Dams *et al*., Accelerated blood clearance and altered biodistribution of repeated injections of sterically stabilized liposomes. *J. Pharmacol. Exp. Ther.* **292**, 1071–1079 (2000).
41. A. S. Abu Lila, H. Kiwada, T. Ishida, The accelerated blood clearance (ABC) phenomenon: Clinical challenge and approaches to manage. *J. Control. Release* **172**, 38–47 (2013).
42. C. Hartmann, R. Patil, C. P. Lin, M. Niedre, Fluorescence detection, enumeration and characterization of single circulating cells in vivo: Technology, applications and future prospects. *Phys. Med. Biol.* **63**, 01TR01 (2017).
43. E. Zettergren *et al*., Instrument for fluorescence sensing of circulating cells with diffuse light in mice in vivo. *J. Biomed. Opt.* **17**, 037001 (2012).
44. X. Tan *et al*., In vivo flow cytometry of extremely rare circulating cells. *Sci. Rep.* **9**, 3366 (2019).
45. V. Pera *et al*., Diffuse fluorescence fiber probe for in vivo detection of circulating cells. *J. Biomed. Opt.* **22**, 37004 (2017).
46. X. Xie, J. Zhai, E. Bakker, pH independent nano-optode sensors based on exhaustive ion-selective nanospheres. *Anal. Chem.* **86**, 2853–2856 (2014).
47. J. M. Dubach, E. Lim, N. Zhang, K. P. Francis, H. Clark, In vivo sodium concentration continuously monitored with fluorescent sensors. *Integr. Biol.* **3**, 142–148 (2011).
48. K. Seiler *et al*., Characterization of sodium-selective optode membranes based on neutral ionophores and assay of sodium in plasma. *Clin. Chem.* **37**, 1350–1355 (1991).
49. M. Shortreed, E. Bakker, R. Kopelman, Miniature sodium-selective ion-exchange optode with fluorescent pH chromoionophores and tunable dynamic range. *Anal. Chem.* **68**, 2656–2662 (1996).
50. X. Xie, E. Bakker, Ion selective optodes: From the bulk to the nanoscale. *Anal. Bioanal. Chem.* **407**, 3899–3910 (2015).
51. X. Xie, I. Szilagyi, J. Zhai, L. Wang, E. Bakker, Ion-selective optical nanosensors based on solvatochromic dyes of different lipophilicity: From bulk partitioning to interfacial accumulation. *ACS Sens.* **1**, 516–520 (2016).
52. K. W. Dunn, S. Mayor, J. N. Myers, F. R. Maxfield, Applications of ratio fluorescence microscopy in the study of cell physiology. *FASEB J.* **8**, 573–582 (1994).
53. X. Huang *et al*., Ratiometric optical nanoprobes enable accurate molecular detection and imaging. *Chem. Soc. Rev.* **47**, 2873–2920 (2018).
54. R. Y. Tsien, M. Poenie, Fluorescence ratio imaging: A new window into intracellular ionic signaling. *Trends Biochem. Sci.* **11**, 450–455 (1986).
55. T. M. Allen, A. Chonn, Large unilamellar liposomes with low uptake into the reticuloendothelial system. *FEBS Lett.* **223**, 42–46 (1987).
56. A. Gabizon, D. Papahadjopoulos, Liposome formulations with prolonged circulation time in blood and enhanced uptake by tumors. *Proc. Natl. Acad. Sci. U.S.A.* **85**, 6949–6953 (1988).
57. D. A. Giljohann *et al*., Gold nanoparticles for biology and medicine. *Angew. Chem. Int. Ed. Engl.* **49**, 3280–3294 (2010).
58. W. Gao *et al*., Surface functionalization of gold nanoparticles with red blood cell membranes. *Adv. Mater.* **25**, 3549–3553 (2013).
59. A. S. Smith *et al*., Myosin IIA interacts with the spectrin-actin membrane skeleton to control red blood cell membrane curvature and deformability. *Proc. Natl. Acad. Sci. U.S.A.* **115**, E4377–E4385 (2018).
60. E. M. Pasini *et al*., In-depth analysis of the membrane and cytosolic proteome of red blood cells. *Blood* **108**, 791–801 (2006).
61. H. Bodemann, H. Passow, Factors controlling the resealing of the membrane of human erythrocyte ghosts after hypotonic hemolysis. *J. Membr. Biol.* **8**, 1–26 (1972).
62. M. Silvander, M. Johnsson, K. Edwards, Effects of PEG-lipids on permeability of phosphatidylcholine/cholesterol liposomes in buffer and in human serum. *Chem. Phys. Lipids* **97**, 15–26 (1998).
63. K. H. Chae, Y. M. Jang, Y. H. Kim, O. J. Sohn, J. I. Rhee, Anti-fouling epoxy coatings for optical biosensor application based on phosphorylcholine. *Sens. Actuators B Chem.* **124**, 153–160 (2007).
64. R. Mercado, M. F. Michelis, Severe sodium depletion syndrome during lithium carbonate therapy. *Arch. Intern. Med.* **137**, 1731–1733 (1977).
65. S. Lippmann, H. Wagemaker, D. Tucker, A practical approach to management of lithium concurrent with hyponatremia, diuretic therapy and/or chronic renal failure. *J. Clin. Psychiatry* **42**, 304–306 (1981).
66. E. J. Brown, W. A. Frazier, Integrin-associated protein (CD47) and its ligands. *Trends Cell Biol.* **11**, 130–135 (2001).
67. S. Jaiswal *et al*., CD47 is upregulated on circulating hematopoietic stem cells and leukemia cells to avoid phagocytosis. *Cell* **138**, 271–285 (2009).
68. P.-A. Oldenborg *et al*., Role of CD47 as a marker of self on red blood cells. *Science* **288**, 2051–2054 (2000).
69. J. E. Tengood, R. J. Levy, S. J. Stachelek, The use of CD47-modified biomaterials to mitigate the immune response. *Exp. Biol. Med. (Maywood)* **241**, 1033–1041 (2016).
70. F. L. Willekens *et al*., Hemoglobin loss from erythrocytes in vivo results from spleen-facilitated vesiculation. *Blood* **101**, 747–751 (2003).
71. A. S. Said, S. C. Rogers, A. Doctor, Physiologic impact of circulating RBC microparticles upon blood-vascular interactions. *Front. Physiol.* **8**, 1120 (2018).
72. F. L. A. Willekens *et al*., Liver Kupffer cells rapidly remove red blood cell-derived vesicles from the circulation by scavenger receptors. *Blood* **105**, 2141–2145 (2005).
73. R. Cánovas, S. Padrell Sánchez, M. Parrilla, M. Cuartero, G. A. Crespo, Cytotoxicity study of ionophore-based membranes: Toward on-body and in vivo ion sensing. *ACS Sens.* **4**, 2524–2535 (2019).
74. J. D. Brain, J. D. Blanchard, J. Heyder, S. F. Wolfthal, B. D. Beck, Relative toxicity of di(2-ethylhexyl) sebacate and related compounds in an in vivo hamster bioassay. *Inhal. Toxicol.* **8**, 579–593 (1996).
75. G. Rong, S. R. Corrie, H. A. Clark, In vivo biosensing: Progress and perspectives. *ACS Sens.* **2**, 327–338 (2017).